

# A photoinduced metallic phase of monoclinic vanadium dioxide.

Vance R. Morrison<sup>1</sup>, Robert. P. Chatelain<sup>1</sup>, Kunal L. Tiwari<sup>1</sup>,  
Ali Hendaoui<sup>2</sup>, Andrew Bruhács<sup>1</sup>, Mohamed Chaker<sup>2</sup>, Bradley J. Siwick<sup>1\*</sup>

<sup>1</sup>Departments of Physics and Chemistry, Center for the Physics of Materials, McGill University  
801 Sherbrooke St. West, Montreal, QC Canada

<sup>2</sup>INRS EMT, Varennes, QC, J3X 1S2, Canada

\*To whom correspondence should be addressed; E-mail: [bradley.siwick@mcgill.ca](mailto:bradley.siwick@mcgill.ca).

The complex interplay between several active degrees of freedom (charge, lattice, orbital and spin order) is thought to determine the electronic properties of many oxides, but the respective role of the various contributions is often extremely difficult to determine. Vanadium dioxide ( $\text{VO}_2$ ) is a particularly notorious example. Here we report on combined ultrafast electron diffraction (UED) and infrared transmissivity experiments in which we directly watch and separate the lattice and charge density reorganizations that are associated with the optically-induced semiconductor-metal transition (SMT) in  $\text{VO}_2$ . These studies have uncovered a previously unreported photoinduced transition to a metastable state with the periodic lattice distortion (PLD) characteristic of the insulator intact, but differing by a 1D rearrangement of charge density along the octahedrally coordinated vanadium dimer chains and a transition to metal-like mid IR optical properties. The results demonstrate that UED is capable of following details of both lattice and electronic

## structural dynamics on the ultrafast timescale.

Understanding the pathways through which microscopic interactions lead to the emergent properties of materials is the central problem of condensed matter physics. Collective phases affected by *multiple* collaborating or competing interactions (1–3) have provided a great challenge in this respect. The development of new methods (both experimental and theoretical) that are able to parse the mechanistic role(s) of several active interacting degrees of freedom are essential to developing an understanding of the properties of such phases. In this article we demonstrate that dramatic recent improvements in ultrafast electron diffraction instrumentation (4–7) provides such a capability by addressing the nature of the much debated semiconductor to metal transition (SMT) in VO<sub>2</sub> (8).

At approximately 343 K, VO<sub>2</sub> undergoes a first order transition between two crystalline phases (Fig. 1A). This structural phase transition (SPT) is accompanied by a dramatic change in conductivity; as much as 5 orders of magnitude in high quality single crystals (9). The high temperature phase, Figure 1A left, is metallic with a rutile crystalline structure (*R*, P4<sub>2</sub>/mnm). The low temperature phase, Figure 1A right, is characterized by semiconducting electronic behavior ( $E_g \sim 0.6$  eV) and monoclinic structure (M1, P2<sub>1</sub>/c). The SPT may be understood roughly as the advent of a charge density wave along the rutile *c*-axis with wave vector  $2\vec{c}_R$ , which leads to a doubling of unit cell along this direction. This periodic lattice distortion (PLD) dimerizes vanadium atoms along the  $\vec{c}_R$  direction, spaced by 2.85 Å in the high temperature phase, into alternating V-V separations of 2.62 Å and 3.16 Å. The dimers are also rotated slightly with respect to  $\vec{c}_R$ .

A long-standing challenge to understanding this SMT has been to determine the relative role of electron-lattice interactions (lattice and charge order) and electron-electron interactions (dynamical correlations and orbital selection) to the change in properties and the nature of the semiconducting phase (10–15). Here we address this question directly by making use of the orders-of-magnitude beam brightness enhancement provided by radio-frequency compressed ultrafast electron diffraction (16) in combination with time-resolved IR transmittance measurements to interrogate both structure and electronic properties. The combined approach makes it possible to map the reorganization of the VO<sub>2</sub> unit

cell *during* the optically induced transition (17, 18) in unprecedented detail while simultaneously determining electronic properties. The results unambiguously demonstrate a photoinduced transformation to a long-lived state with metal-like mid IR optical properties and the PLD (or charge density wave order) of the semiconducting M1 phase intact. This state differs from the equilibrium rutile metal crystallographically, and in that it only involves a 1D reorganization of charge density rather than a transition to the isotropic 3D electronic state of the high temperature phase (19, 20).

In these experiments pulsed-laser deposition grown polycrystalline VO<sub>2</sub> films (Figs. 1B, 1C) (21), initially in the low temperature M1 phase (at  $\sim 310\text{K}$ ), are subject to optical (800nm) excitation with 35 fs laser pulses. The time-dependence of the changes in structure and electronic properties following optical excitation of the material are determined using pump-probe UED and time resolved IR transmittance measurements (22). The time-resolved transmission electron powder diffraction data obtained using UED (Fig. 2) provides an extremely rich and detailed view of the structural dynamics following photoexcitation. Raw (background subtracted) UED data for 20 ps following photoexcitation at an intermediate pump fluence of 20 mJ/cm<sup>2</sup> is shown in Fig. 2A. Of particular note are several weak reflections ( $30\bar{2}$ ,  $12\bar{2}$  and  $31\bar{3}$ , indicated by red lines), which are allowed in the M1 phase due to the PLD and the doubling of the unit cell along  $\vec{c}_R$ , but not in the *R* phase. The intensity of these peaks clearly decreases with time following photoexcitation, which is indicative of the optically induced SPT that occurs in some of the sample at this fluence. Similar observations were made in previous ultrafast structural measurements on VO<sub>2</sub> which identified a sub 500 fs timescale for aspects of the SPT (23, 24). Beyond these specific peaks, however, photoexcitation induces changes in diffracted intensity over the entire scattering vector range shown. This is clearly evident in Fig. 2B where the time-dependent difference in diffracted intensity with respect to negative pump-probe delays (i.e. before photoexcitation) is plotted. The presence of multiple time scales can be seen clearly in Fig. 2C which shows the time dependent intensity of several diffraction features labeled in Fig. 2A. After photoexcitation at 20 mJ/cm<sup>2</sup> there is a fast,  $310\pm 160$  fs, decrease in the intensity of diffraction peaks associated with the PLD (e.g.,  $30\bar{2}$ ), followed by a slow  $1.6\pm 0.2$  ps time constant increase in the intensity of most peaks in the range

$s < 0.45 \text{ \AA}^{-1}$  that are present for both phases (e.g., the 220 and 200 features). These are the only two ultrafast time constants observed in the data up to 10 ps.

The amplitude of these two qualitatively distinct diffraction signatures each scale linearly with fluence, but have different slopes and threshold fluences:  $9 \text{ mJ/cm}^2$  for fast pump-induced changes to peaks associated with the PLD in the M1 phase and  $2 \text{ mJ/cm}^2$  for the slow changes. At pump fluences below  $\sim 9 \text{ mJ/cm}^2$  (hatched region in Fig. 2D) there is no change to the intensity of diffraction peaks associated with the PLD in the M1 phase. Inset in Fig. 2D are time-resolved IR transmittance curves at 5 microns (0.25 eV) for the  $\text{VO}_2$  film at several pump fluences below  $9 \text{ mJ/cm}^2$ . These curves show a persistent decrease in IR transmissivity that increases with pump fluence and reaches an amplitude of  $>99\%$  by  $3.7 \text{ mJ/cm}^2$ . This observation is in quantitative agreement with previous experiments using multi-THz spectroscopy on pulsed laser deposition grown  $\text{VO}_2$  films (25, 26), and is indicative of a (partial) transition to a state with metallic-like AC conductivity at a threshold pump-fluence of approximately  $2 \text{ mJ/cm}^2$ .

We isolate the full spectrum of diffracted intensity changes that correspond to the fast and slow components in the time-domain by choosing reference time points for computing the intensity differences that separate these dynamics, i.e.,  $t = -1 \text{ ps}$  in Fig. 2E (fast dynamics) and  $t = 2 \text{ ps}$  in Fig. 2F (slow dynamics). It is important to note that unlike the fast dynamics in Fig. 2E, the slow dynamics are dominated by increases in peak intensity over a limited range of scattering vector ( $s < 0.45 \text{ \AA}^{-1}$ ) for which electron scattering is known to be particularly sensitive to the valence charge distribution (27, 28). In addition, these slow dynamics are absent for reflections whose reciprocal lattice vector is perpendicular to  $\vec{c}_R$  ( $h_M = 0$ ), as indicated with grey dotted lines in Fig. 2. This observation unambiguously establishes that electron structure factors orthogonal to  $\vec{c}_R$  are largely unaffected by the slow process; i.e. the slow process corresponds to a 1D modification of the electrostatic crystal potential in the octahedrally coordinated vanadium chains oriented along  $\vec{c}_R$ .

The two diffraction signatures described above represent qualitatively distinct structural reorganizations within  $\text{VO}_2$  following photoexcitation. This can be understood by computing the pump-induced changes to the radial pair distribution function (PDF) (29)

directly from the observed changes in diffracted intensity shown in Fig. 2E and F. These curves, shown in Fig. 3A and B, represent the time-dependent difference in the radial autocorrelation function of the crystal potential with respect to the reference time point. The computed difference PDF for the fast dynamics is shown in Fig. 3A and provides a straight forward structural interpretation for this signal. The positive growing feature (II) corresponds to increased correlation at the *R* phase V-V bond length, 2.85 Å, while the adjacent negative going features (I, III) represent a reduction at the dimer (2.62 Å) and unpaired (3.16 Å) distances of the *M1* phase as indicated in Fig. 1. Thus, the fast dynamics correspond to non-thermal melting of the PLD in a fluence dependent fraction of crystallites. In these crystallites the vanadium atomic positions relax to their equilibrium *R*-phase separation on the 300 fs timescale. Extrapolating the linear scaling of these dynamics with fluence indicates that  $\sim 43$  mJ/cm<sup>2</sup> is required to melt the PLD (CDW order) in the entire film. Pump fluences  $< 9$  mJ/cm<sup>2</sup> are insufficient to initiate this non-thermal SPT in any crystallites/volume, and leave the PLD and *M1* crystal structure completely intact. Below this  $\sim 9$  mJ/cm<sup>2</sup> threshold only the slow dynamics is observed (Figs. 2F and S4). The diffraction signature of these dynamics is identical below and above the SPT threshold, demonstrating that the slow and fast components represent distinct transitions occurring in different crystallites/volumes due to the heterogeneity of these pulsed laser deposition samples.

In contrast to the above, the slower dynamics do not correspond to a structural rearrangement of the lattice (which result in a conservation of diffracted intensity like that seen for the fast dynamics in Fig 2E). The difference PDF (Fig. 3B) for the slow changes is dominated by negative going features at 1.3 Å (IV) and 4.4 Å (VI), equal to half the V-V dimer bondlength and the undimerized V-V separation plus half the V-V dimer bondlength respectively (Fig. 1A). Positive going changes are also observed at around 1.9 Å (V), the average V-O separation in the octahedron, and at  $< 0.8$  Å. These observations are consistent with a collective reorganization of valence charge density in the *M1* phase that increases the electron density in the vanadium dimers bonds while decreasing the electrostatic potential on primarily the oxygen atoms; an effective modification of the atomic scattering factors.

Previous theoretical work on vanadium dioxide has focused on the behaviour and occupancy of the three bands formed from hybridized V-3d/O-2p states of  $t_{2g}$  symmetry (Fig 4A) as the determining factor in the electronic properties of VO<sub>2</sub> (10, 13–15). The orientation of the localized  $d$ -orbitals from which these bands are formed are shown in Fig. 4B. The  $d_{xy}$  (also referred to as  $d_{\parallel}$ ) and  $d_{xz}$  orbitals mediate sigma and pi type interactions between vanadiums along  $\vec{c}_R$  respectively. The  $d_{yz}$  orbital is oriented orthogonal to  $\vec{c}_R$ . There is broad agreement in the high temperature phase these three bands almost completely overlap at the Fermi level (13, 14), as shown in Fig. 4A-i. This results in roughly equal occupancy in these bands and a nearly isotropic electronic state (19, 20). It has been suggested that the PLD in the  $M1$  phase splits the  $d_{\parallel}$  states into bonding and anti-bonding combinations sufficiently to open an insulating gap (10), but density functional theory calculations using the local density approximation maintain significant density of states at the Fermi level in the  $M1$  phase (13, 14) as shown in Fig. 4A-ii (30, 31)

Recent work using cluster dynamical mean field theory points to dynamical electron-electron correlations acting in collaboration with the PLD as being responsible for the insulating properties of the  $M1$  phase (Fig. 4) (14, 15). The results presented here support this view. We have demonstrated that optical excitation can induce a long lived state with IR transmissivity like that of the metallic phase (i.e., collapse of the optical bandgap to below 0.25 eV) in the absence of a SPT. This state has the PLD of the insulating phase intact, but the valence charge distribution significantly altered. The nature of the changes in charge density can be understood from the symmetry of the changes in diffraction presented in Fig. 2F, the orbitals shown in Fig. 4B and the difference PDF in Fig. 3B. The negative going feature at 1.3 Å and 4.4 Å in Fig. 3B suggests an increase in the filling of the  $d_{xy}$  subshell that mediate V-V dimer bonds. The positive going features at 0.8 Å and 1.9 Å suggest reduced filling of the  $d_{xz}$  subshell, which reduces charge density on the V and O atoms in the octahedral chains. The  $d_{yz}$  states oriented orthogonal to  $\vec{c}_R$ , which are understood to be unoccupied in semiconducting VO<sub>2</sub> (15, 20), remain unchanged. Thus, optical excitation with fluences below the threshold required to melt the PLD drives a 1D redistribution of occupancy in the  $d_{xy}$  and  $d_{xz}$  subshells, not a transformation to the isotropic state of the equilibrium metal. Suppression of correlation induced splitting into

upper (UHB) and lower (LHB) Hubbard bands, either preferentially in the  $d_{xz}$  band (Fig. 4A iv) or in both  $d_{xz}$  and  $d_{xy}$  shells (Fig. 4A ii), could lead to such a reorganization. The first case represents an optically induced orbital selective transition with a mixture of localized ( $d_{xy}$ ) and itinerant ( $d_{xz}$ ) behaviour (32). The picosecond timescale of this transformation in addition to its long-lived nature suggests that the increased vibrational excitation of the lattice due to carrier relaxation (e-ph coupling) is a key factor in both inducing and maintaining the reorganization. The nonequilibrium population of excited carriers relax in  $\sim 1$ ps in thin pulsed laser deposition grown  $\text{VO}_2$  films (25). However, the present measurements cannot rule out the possibility of other mechanisms affecting this stability, including kinetic trapping of the valence charge reorganization. Here a tentative connection can be made to earlier work which identified metal-like phases of  $\text{VO}_2$  with properties unlike that of the rutile, high-temperature metal. Qazilbash *et al.* observed the emergence of nanoscale correlated metallic domains with electronic properties unlike those of the rutile metal near the transition temperature (33, 34). The lattice structure of these puddles was not identified. Additionally, the work of Nag *et al.* demonstrated that the SMT and SPT can occur non-congruently when initiated thermally, suggesting the presence of a metal-like, M1 phase of  $\text{VO}_2$  (35). The correlated metallic state observed in the thermally activated phase transition and the M1 phase metastable state accessed optically here may be related.

The results presented here have several important implications to our understanding of the hierarchy of roles for electron-lattice and electron-electron degrees of freedom in determining the properties of semiconducting  $\text{VO}_2$ . The profound decoupling of the SMT in mid IR optical properties and the SPT induced through optical excitation indicates that the PLD of the M1 phase is insufficient to fully explain the semiconducting gap. From the perspective of the dramatic change in electronic properties, the principle role of the PLD is to alter the accessibility of the bands formed by states of  $d_{xy}$  symmetry (10). With the PLD in place these states are depopulated, and the highest energy occupied bands have a 1D character and are susceptible to further electronic ordering. The isotropic electronic character of the equilibrium rutile metal (20) cannot be realized with the PLD intact. Finally, the large threshold excitation fluence for the SPT compared to that for

the observed electronic reorganization demonstrates that the latent heat of the first order phase transition at  $\sim 340\text{K}$  is dominated by the SPT rather than the electronic transition.

In summary, we have demonstrated that substantial advances in UED have provided the capability to simultaneously probe the dynamics of both lattice structure and charge density on the femtosecond time scale. This provided new insights on the SMT in  $\text{VO}_2$ , uncovering a novel optically accessible state. Based on this study, UED is now positioned to provide deep insights into the nature of other strongly correlated materials through the disparate concurrent responses of active degrees of freedom in the time domain. Further, our results have relevance to the study of the interplay between valence charge and lattice structure in molecular and materials chemistry.

## References

1. M. Imada, A. Fujimori, *Reviews of Modern Physics* **70**, 1039 (1998).
2. E. Dagotto, *Science* **309**, 257 (2005).
3. P. A. Lee, X.-G. Wen, *Reviews of Modern Physics* **78**, 17 (2006).
4. B. J. Siwick, J. R. Dwyer, R. E. Jordan, R. J. D. Miller, *Science* **302**, 1382 (2003).
5. C.-Y. Ruan, Y. Murooka, R. K. Raman, R. A. Murdick, *Nano letters* **7**, 1290 (2007).
6. G. Sciaini, R. J. D. Miller, *Reports on Progress in Physics* **74**, 096101 (2011).
7. M. Gao, *et al.*, *Nature* **496**, 343 (2013).
8. L. Whittaker, C. J. Patridge, S. Banerjee, *The Journal of Physical Chemistry Letters* **2**, 745 (2011).
9. C. Berglund, H. Guggenheim, *Physical Review* **238**, 1022 (1969).
10. J. Goodenough, *Journal of Solid State Chemistry* **500**, 490 (1971).
11. A. Zylbersztein, N. Mott, *Physical Review B* **11**, 4383 (1975).



12. R. Wentzcovitch, W. Schulz, P. Allen, *Physical Review Letters* **72**, 3389 (1994).
13. V. Eyert, *Ann. Phys. (Leipzig)* **11**, 650 (2002).
14. S. Biermann, A. Poteryaev, A. Lichtenstein, A. Georges, *Physical Review Letters* **94**, 026404 (2005).
15. C. Weber, *et al.*, *Physical Review Letters* **108**, 256402 (2012).
16. R. P. Chatelain, V. R. Morrison, C. Godbout, B. J. Siwick, *Applied Physics Letters* **101**, 081901 (2012).
17. A. Cavalleri, T. Dekorsy, H. Chong, J. Kieffer, R. Schoenlein, *Physical Review B* **70**, 161102 (2004).
18. S. Wall, *et al.*, *Physical Review B* **87**, 115126 (2013).
19. T. C. Koethe, *et al.*, *Physical Review Letters* **97**, 116402 (2006).
20. M. W. Haverkort, *et al.*, *Physical Review Letters* **95**, 196404 (2005).
21. A. Hendaoui, N. Émond, S. Dorval, M. Chaker, E. Haddad, *Current Applied Physics* **13**, 875 (2013).
22. Materials and methods can be found in the supplementary material located at the end of this document.
23. A. Cavalleri, *et al.*, *Physical Review Letters* **87**, 237401 (2001).
24. P. Baum, D.-S. Yang, A. H. Zewail, *Science* **318**, 788 (2007).
25. A. Pashkin, *et al.*, *Physical Review B* **83**, 195120 (2011).
26. T. L. Cocker, *et al.*, *Physical Review B* **85**, 155120 (2012).
27. J. M. Zuo, *Reports on Progress in Physics* **67**, 2053 (2004).
28. J.-C. Zheng, Y. Zhu, L. Wu, J. W. Davenport, *Journal of Applied Crystallography* **38**, 648 (2005).

29. A. M. M. Abeykoon, *et al.*, *Zeitschrift für Kristallographie* **227**, 248 (2012).
30. A. S. Belozerov, M. A. Korotin, V. I. Anisimov, A. I. Poteryaev, *Physical Review B* **85**, 045109 (2012).
31. R. Sakuma, T. Miyake, F. Aryasetiawan, *J. Phys.: Condens. Matter* **21**, 064226 (2009).
32. Y. Yao, *et al.*, *Modern Physics Letters B* **27**, 1330015 (2013).
33. M. M. Qazilbash, *et al.*, *Physical Review B* **83**, 165108 (2011).
34. M. M. Qazilbash, *et al.*, *Science* **318**, 1750 (2007).
35. J. Nag, R. F. Haglund, E. Andrew Payzant, K. L. More, *Journal of Applied Physics* **112**, 103532 (2012).
36. This work was supported by the Canada Foundation for Innovation (CFI), Canada Research Chairs (CRC) program, the Natural Sciences and Engineering Research Council of Canada (NSERC) and Fonds de Recherche du Québec-Nature et Technologies (FQNT). R.P.C. and V.M. gratefully acknowledges the support of NSERC PGS-D and CGS-D fellowships. Finally, the authors would like to thank C. Weber for insightful discussion regarding the contemporary theoretical treatment of the electronic structure of VO<sub>2</sub>.

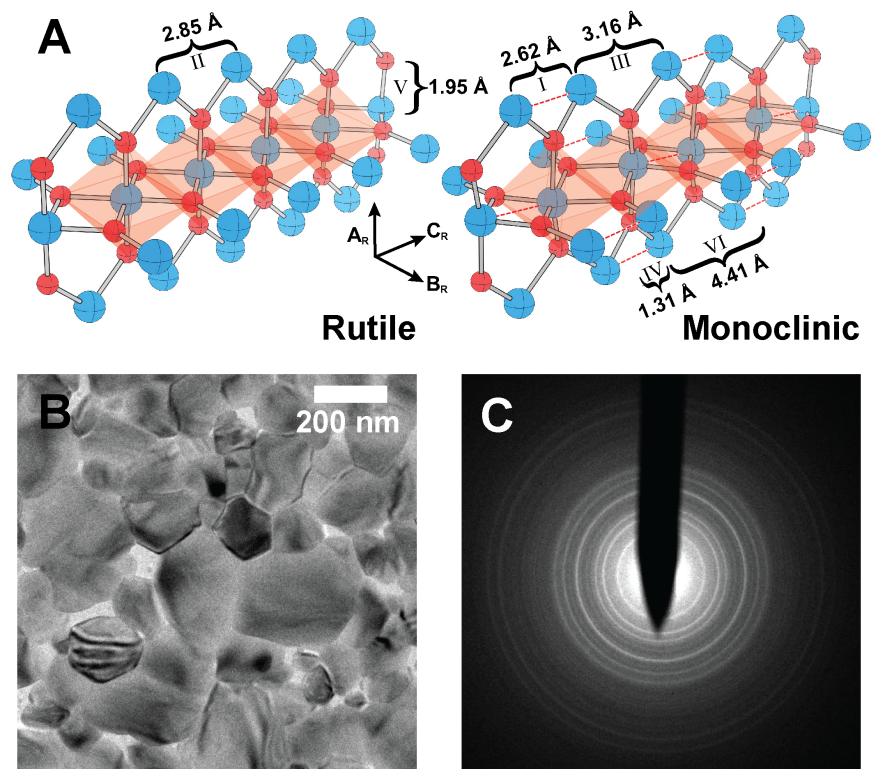


Figure 1: A) The structure of rutile VO<sub>2</sub> (left) and monoclinic VO<sub>2</sub> (right). B) Transmission electron microscopy image of the pulsed laser deposition grown VO<sub>2</sub> sample used in these studies. C) Example electron powder diffraction pattern of the monoclinic phase.

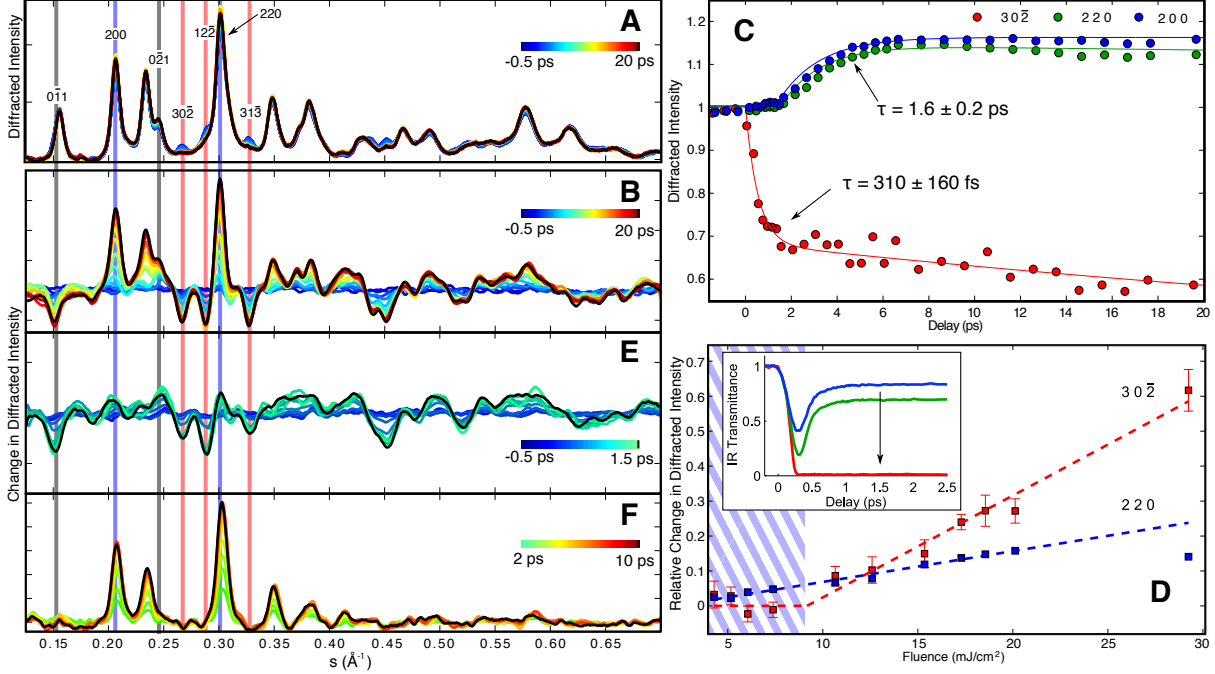


Figure 2: Structural dynamics during the SMT in  $\text{VO}_2$ . A) Raw, background subtracted, UED data from 0-20 ps. Red vertical lines indicate several weak reflections allowed in the M1 phase due to the PLD but not in the R-phase. Blue lines indicate several peaks present in both equilibrium phases. The grey lines indicate peaks for which  $h_M = 0$ . B) Overall diffraction difference spectrum from -0.5 to 20 ps, C) Time resolved diffraction peak intensity showing fast ( $\sim 300\text{fs}$ ) and slow ( $\sim 1.6\text{ ps}$ ) dynamics respectively for peaks indicated by red and blue vertical lines in the diffraction spectra (leftmost panels). The dashed line demarks a delay of 1.5 ps and acts as guide to the eye. D) Fluence dependence of the fast and slow signal amplitudes as measured for the  $(30\bar{2})$  and  $(220)$  peaks shown in C). The range of fluences for which no SPT is observed is indicated by the hatched region. Inset) Time resolved IR ( $5\ \mu\text{m}$ ,  $0.25\ \text{eV}$ ) transmissivity in this hatched fluence region ( $3.7\ \text{mJ}/\text{cm}^2$  (red),  $2.7\ \text{mJ}/\text{cm}^2$  (green) and  $1.9\ \text{mJ}/\text{cm}^2$  (blue)) display a persistent decrease to a very long-lived plateau ( $>100\text{ps}$ ). The amplitude of this decrease reaches  $>99\%$  at  $3.7\ \text{mJ}/\text{cm}^2$ , indicating a significant closing of the semiconducting gap and a transition to a metallic-like state. E) Diffraction difference spectrum for the fast dynamics. The change in diffracted intensity from -0.5 ps to 1.5 ps and F) Diffraction difference spectrum for the slow dynamics. The change in diffracted intensity from 2 ps to 10 ps (referenced to 2 ps) is shown.

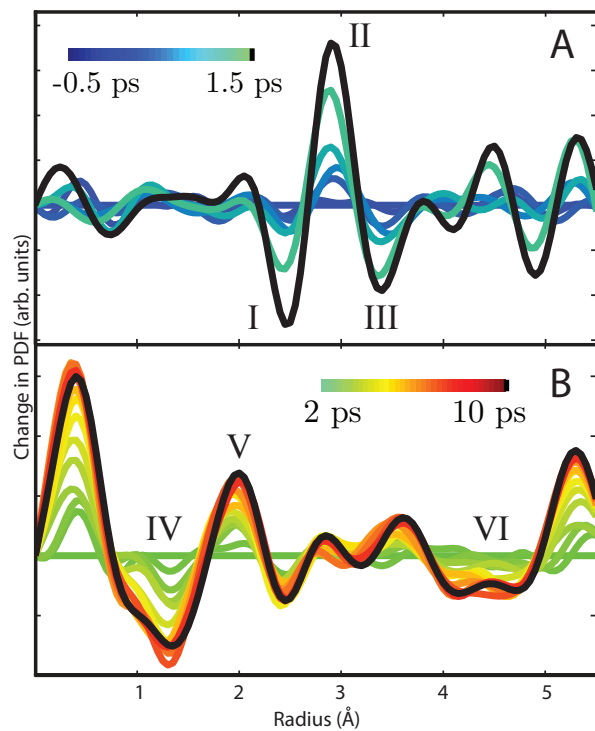


Figure 3: Difference pair distribution functions for the two observed characteristic time scales. A) Difference PDF from -0.5 ps to 1.5 ps referenced to -0.5 ps. B) Difference PDF from 2 ps to 10 ps, referenced to 2 ps. The roman numerals correspond to the distances labeled in Fig 1.

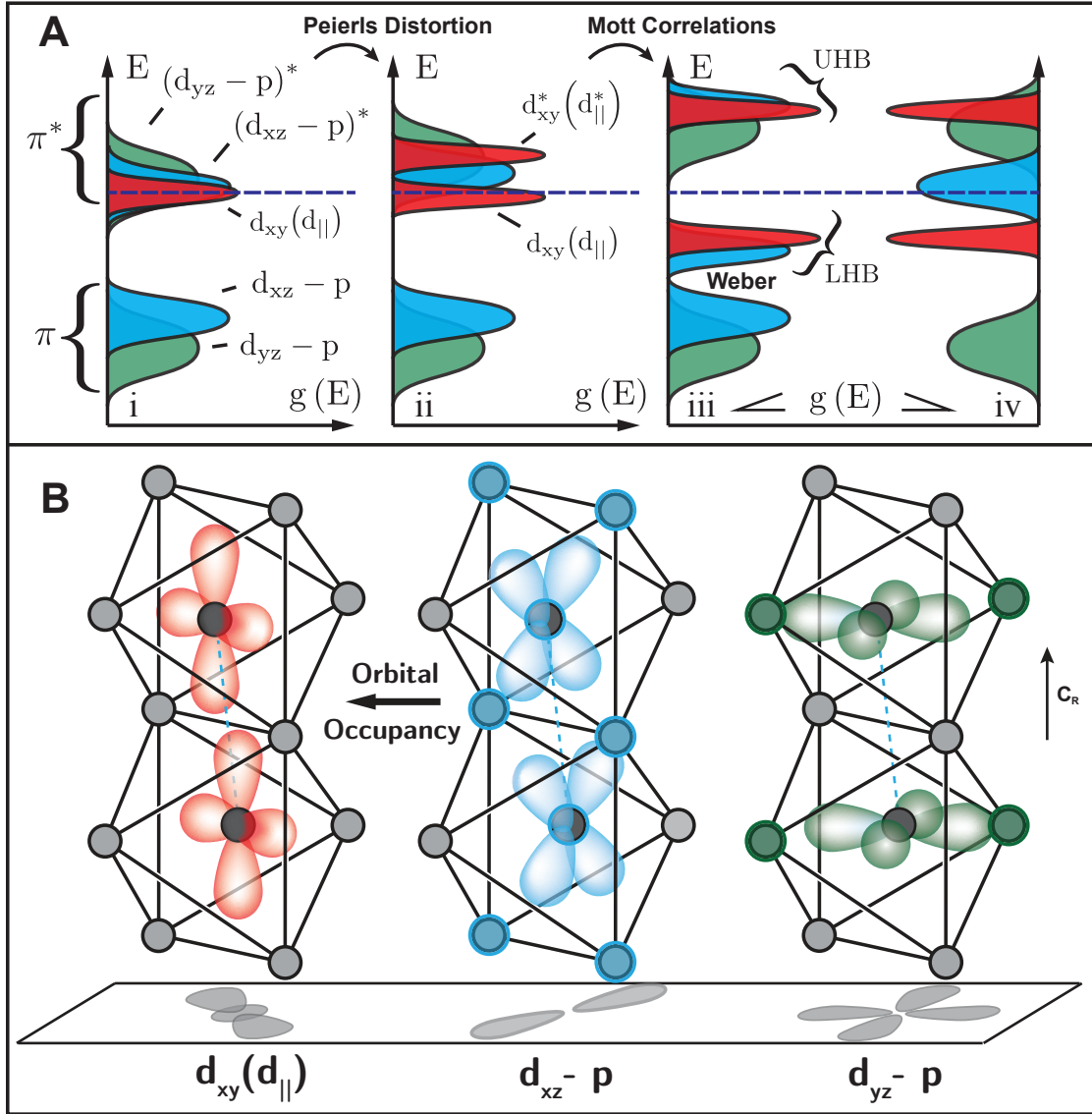


Figure 4: Effective band diagrams of  $\text{VO}_2$  and illustrations of the associated molecular orbitals. A-i) Band diagram for the rutile, metallic phase. A-ii) Modified band diagram as a result of the PLD. A-iii) The effect of el-el correlations as described by Weber et al (15). A-iv) The band diagram resulting from the partial Mott melting of the  $d_{xz}$  band. B) Illustrations of the  $d_{xy}$ ,  $d_{xz}$ , and  $d_{yz}$  molecular orbitals.

## Supplementary Material

The measurements presented here were made on a home built ultrafast electron diffractometer (Fig. S1) employing radio-frequency pulse compression techniques (S1). This approach has very recently been shown to offer dramatic improvements in instrument performance (S2, 16). These techniques allow us to produce compressed electron pulses with  $\sim 10^6$  electrons per pulse with  $\sim 300$  fs time resolution (16).

In these experiments, VO<sub>2</sub> specimens initially in the *M1* phase ( $\sim 310$  K) are photoexcited with 35 fs, 1.55 eV (800 nm) laser pulses at near normal incidence ( $\sim 10$  degrees) with a range of excitation fluences; the evolution of the SMT was then probed after a variable delay time with an ultrashort electron pulse with  $\sim 500,000$  electrons per pulse. These electron pulses were generated through photoemission in a DC, high voltage electron gun with 266 nm laser pulses and accelerating voltages up to 95 kV. Although the diffractometer is capable of operating with a repetition rate of 1 kHz, a delay of 20 ms between pump laser pulses was required before reinitiating the transition in order to allow the samples to completely relax back to the insulating phase. The diffraction pattern (Fig. S2) produced at each delay is the result of approximately 50 individual fifteen second exposures and was detected on a Gatan Ultrascan 1000, a phosphor coated CCD with near single electron detection capabilities.

In addition to the ultrafast electron diffraction measurements performed, ultrafast infrared transmittance measurements were conducted under identical pump-probe conditions. The IR pulses (5  $\mu\text{m}$  wavelength) were generated using difference frequency generation from the signal and idler beams of an IR optical parametric amplifier (S3). The ultrafast mid-IR transmission measurements were made using the femtosecond pulse acquisition spectrometer from Infrared Systems Development, based on 64 pixel Mercury Cadmium Telluride IR detector arrays. The VO<sub>2</sub> samples were held at atmospheric pressure as opposed to the  $10^{-7}$  Torr used for the electron diffraction experiments.

The high-quality stoichiometric polycrystalline vanadium dioxide films used in these measurements were synthesized at the Laboratory of Micro- and Nanofabrication facility at INRS by means of reactive pulsed laser deposition process. A pure (99.95%) vanadium

target was used with a KrF excimer laser ( $\lambda = 248$  nm) in an oxygen environment with a pressure of 15 mTorr and substrate temperature of 500 °C (S4, 21). The samples were 70 nm thick and deposited on 50 nm thick amorphous silicon nitride windows. Temperature dependent resistivity curves of the samples used are shown in Fig. S3 and display the characteristic hysteretic behaviour of VO<sub>2</sub> with a hysteresis width of 10 K.

## References

- S1. T. van Oudheusden, *et al.*, *Journal of Applied Physics* **102**, 093501 (2007).
- S2. M. Gao, *et al.*, *Optics Express* **20**, 799 (2012).
- S3. R. A. Kaindl, *et al.*, *Journal of the Optical Society of America B* **17**, 2086 (2000).
- S4. A. Hendaoui, N. Émond, M. Chaker, E. Haddad, *Applied Physics Letters* **102**, 061107 (2013).



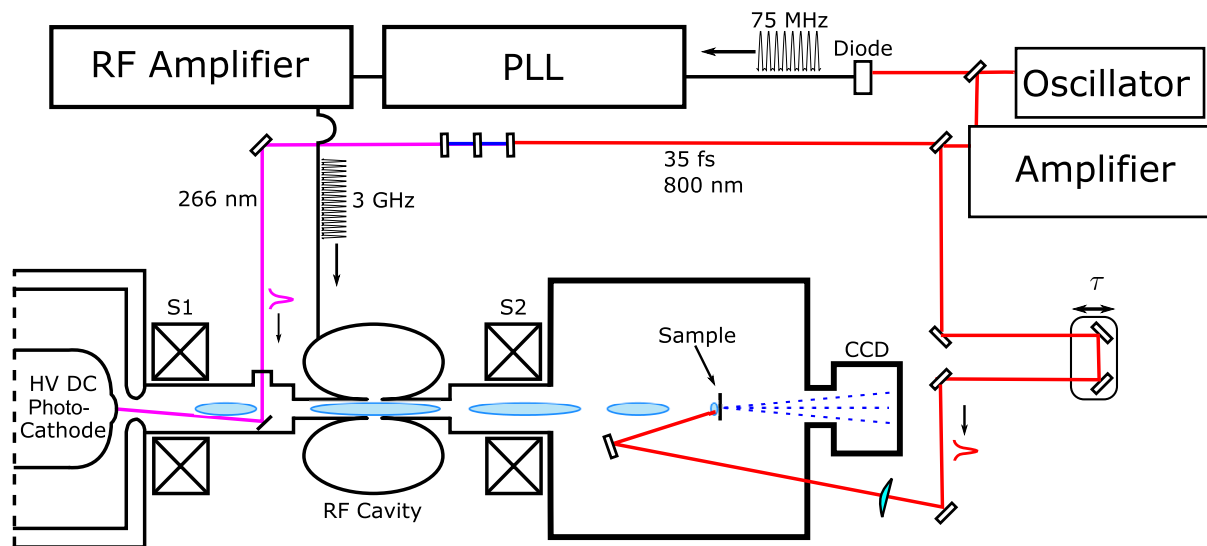


Figure S1: Schematic diagram of the ultrafast electron diffractometer including the synchronization electronics and the chirped pulse amplification laser system. The sample is pumped with 35 fs, 800 nm laser pulses, while third harmonic generation is used to produce 266 nm, UV pulses. A fast photo-diode is used to detect the timing of the pulses from the ultrafast oscillator; a phase-locked loop (PLL) is then used to produce synchronized RF pulses which are then amplified by an RF amplifier. These pulses then drive the RF compression cavity. Two magnetic lenses, S1 and S2, are used to collimate the electron beam as it exits the electron gun, and then to focus the beam at the CCD detector.

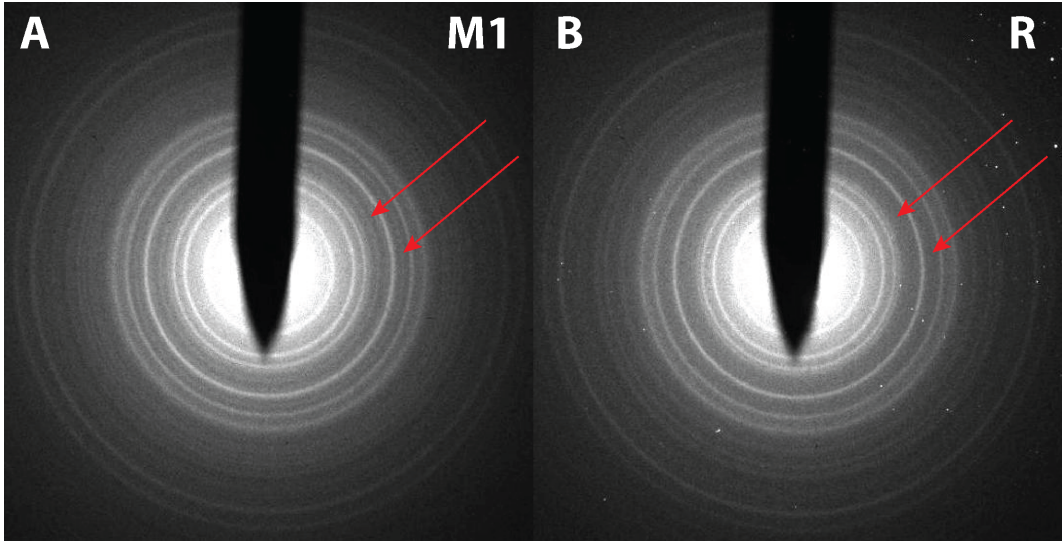


Figure S2: Diffraction patterns of low temperature (A) and high temperature (B) phases of  $\text{VO}_2$ . The red arrows indicate the disappearance of diffraction features which are present in the M1 phase, but not allowed by symmetry in the R phase. The shadow in the center of the images is a beam block used to prevent the main electron beam from saturating the CCD.

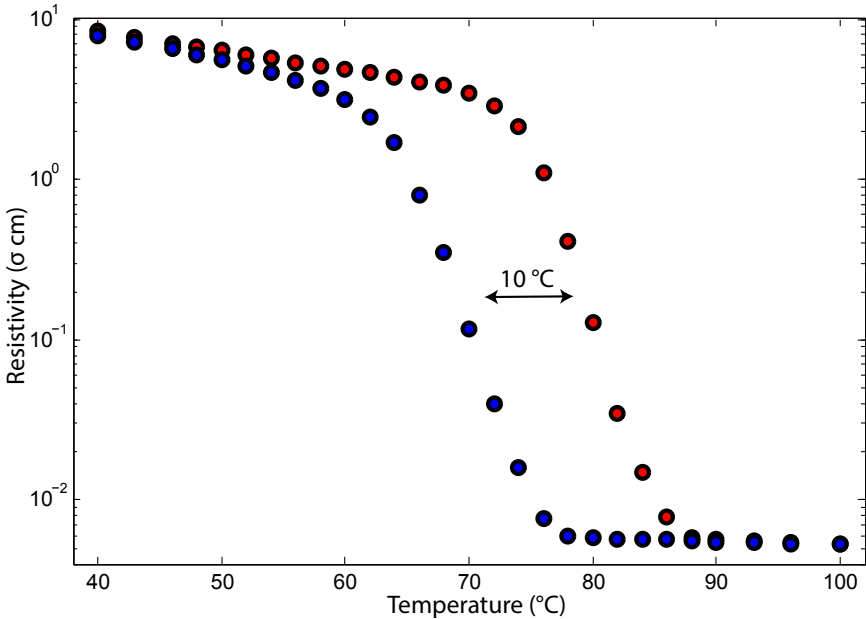


Figure S3: Temperature dependent resistivity curve of the IMT in the thin film  $\text{VO}_2$  samples used. The hysteresis width is  $10\text{ }^\circ\text{C}$  with increasing temperature shown in red and decreasing temperature shown in blue.

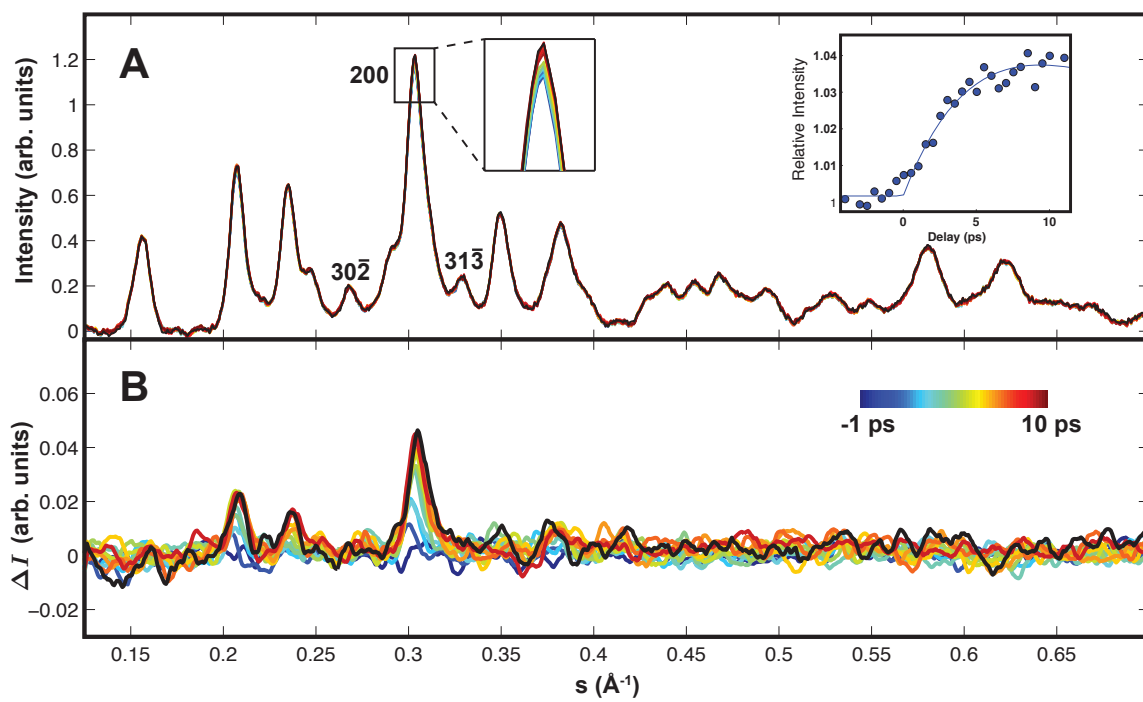


Figure S4: A) Time resolved, background subtracted, diffraction data from 0 ps to 10 ps and an excitation fluence of 6.1 mJ/cm<sup>2</sup>. Inset) Time resolved intensity of the 220 reflection. B) Time resolved change in diffracted intensity shown in A). No decrease is seen in the  $30\bar{2}$  and  $31\bar{3}$  reflections, indicating that the PLD remains intact. In addition, no changes are observed in the  $s > 0.5 \text{ \AA}^{-1}$  region.